Nanoporous Carbon Supercapacitors in an Ionic Liquid: A Computer Simulation Study

Youngseon Shim[†,‡,⊥] **and Hyung J. Kim**[†,§,*]

[†]Department of Chemistry, Carnegie Mellon University, Pittsburgh, Pennsylvania 15213, [‡]Department of Chemistry, Seoul National University, Seoul 151-747, Korea, and [§]School of Computational Sciences, Korea Institute for Advanced Study, Seoul 130-722, Korea. [⊥]Present address: Seoul National University.

ABSTRACT Supercapacitors composed of carbon nanotube (CNT) micropores in the room-temperature ionic liquid (RTIL) 1-ethyl-3-methylimidazolium tetrafluoroborate ($EMI^+BF_4^-$) are studied *via* molecular dynamics (MD) computer simulations. It is found that the distribution of RTIL ions inside the micropore varies significantly with the pore size. Internal solvation of small (6,6) and (7,7) CNTs with an electrified interior wall is effected almost exclusively *via* counterions. Surprisingly, these counterions, even though they all have the same charge, lead to a charge density characterized by multiple layers with alternating signs. This intriguing feature is attributed to the extended nature of RTIL ion charge distributions, which result in charge separation through preferential orientation inside the electrified nanotubes. In the case of larger (10,10) and (15,15) CNTs, counterions and co-ions develop multilayer solvation structures. The specific capacitance normalized to the pore surface area is found to increase as the CNT diameter decreases from (15,15) to (7,7). As the pore size further reduces from (6,6) to (5,5), however, the specific capacitance diminishes rapidly. These findings are in excellent agreement with recent experiments with carbon-based materials. A theoretical model based on multiple charge layers is proposed to understand both the MD and experimental results.

KEYWORDS: supercapacitor · electric double layer · ionic liquid · imidazolium ion · carbon nanotube · micropore · molecular dynamics simulations · specific capacitance

Harnessing alternative energies poses one of major challenges to modern science and technology. As the availability of fossil fuels decreases, the conversion of the energy from alternative and preferably renewable sources and its efficient storage are becoming crucial to the sustainability of our civilization. As such, energy conversion and storage is currently the subject of intensive investigation across the board in science and technology.

Electrochemical devices, such as batteries and capacitors, are the best known and perhaps the most promising energy storage systems. Recently, electrical double layer capacitors (EDLCs),[1−5] also known as supercapacitors or ultracapacitors, have received significant experimental scrutiny because they can achieve a higher energy density than conventional capacitors and offer a better power performance than batteries. Two different classes of ionic solutions, that is, aqueous and organic electrolytes, are usually employed for EDLCs. Thanks to their low internal resistance, aqueous electrolytes generally yield a high power density for EDLCs. Their low decomposition voltage ($\lesssim$1 V) nevertheless places a significant limit on the density of the stored energy. Organic electrolytes on the other hand allow a higher cell voltage up to ~2.5 V but their relatively low conductivity leads to a poor power performance compared to aqueous electrolytes. Room-temperature ionic liquids (RTILs) thus provide an attractive alternative to these conventional electrolytes for EDLCs owing to their wide electrochemical window and high ion density as well as good thermal stability and nonvolatility.[6−18]

With a few exceptions,[19,20] there has been virtually no systematic analysis of EDLCs in RTILs at the molecular level with computational methods despite rapidly growing interest in these systems. One good example is the capacitance of micropores, which shows an interesting dependence on the pore size. According to several recent experiments, the specific capacitance of various carbon-based EDLCs increases significantly with decreasing pore size when it is comparable to the size of ions.[11−15] Originally it was conjectured that distortion of the solvation shell of ions inside narrow pores is responsible for the anomalous behavior of the specific capacitance.[12,13] The recent "electric wire-in-cylinder capacitor" (EWCC) model offers additional insight into roles played by counterions inside the micropores.[21,22] EWCC nonetheless is based on a continuum description with counterions modeled as a charged surface/wire and thus misses many

*Address correspondence to hjkim@cmu.edu.

Received for review December 28, 2009 and accepted March 19, 2010.

Published online April 1, 2010.
10.1021/nn901916m

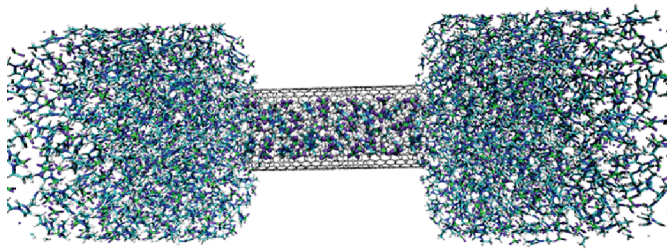

Figure 1. Supercapacitor system composed of a (15,15) CNT as a micropore and $EMI^+BF_4^-$ as an electrolyte. RTIL ions can approach the carbon atoms of the CNT only through the nanotube tunnel due to the presence of a repulsive slab (not shown here) surrounding the nanotube.

molecular aspects of EDLCs. In addition, its applicability becomes considerably restricted when both counterions and co-ions make contributions to capacitance as in, for example, relatively large micropores and mesopores in RTILs. According to our recent molecular dynamics (MD) study, the structure of RTIL cations and anions inside CNTs varies dramatically with the nanotube size; a mere 0.1−0.2 nm increase in the CNT diameter induces marked structural changes, for example, from single-file to zigzag and chiral distributions and from disordered to ordered and back to disordered distributions of RTIL ions.[23] These observations suggest that detailed analysis at the molecular level is needed for both qualitative and quantitative understanding of EDLCs at the nanoscale.

As an initial step toward this goal, we investigate nanoporous supercapacitors in the RTIL $EMI^+BF_4^-$ *via* MD in this paper. We examine the structure of, and charge distributions resulting from, EMI^+ and BF_4^- ions, which interact with a model micropore consisting of a uniformly charged, single-walled CNT in the (*n*,*n*) armchair configuration,[24] surrounded by a slab that repels the solvent (cf. Figure 1). By analyzing the electrode potential as a function of the nanotube surface charge density and diameter, we study the specific capacitance of the micropore and its dependence on the pore size. By extending EWCC,[21,22] we propose an "electric multiple-charge-layer capacitor" (EMLC) description to understand the MD and experimental results, including their differences.

RESULTS AND DISCUSSION

We begin by considering the electric potential of the nanotube supercapacitors in $EMI^+BF_4^-$. We mention at the outset that electronic polarizability[25,26] is not included in our model descriptions[23,27−29] employed for the CNTs and RTIL in the present study. One noticeable artifact arising from this simplification is that the electric potential at the CNT wall varies with the posi-

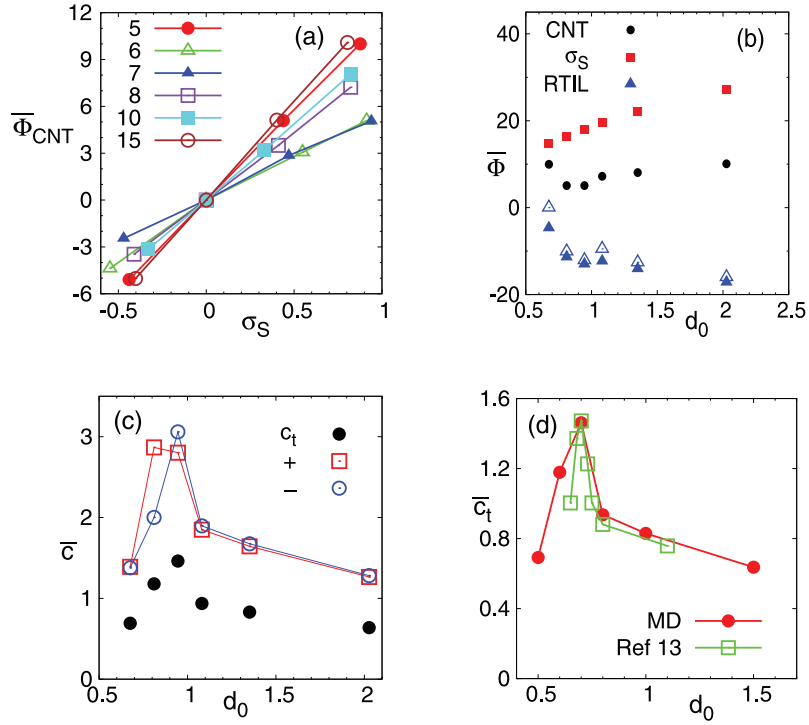

Figure 2. MD results for (a) electrode potential $\bar{\Phi}_{CNT}$, (b) its components $\bar{\Phi}_\sigma$ and $\bar{\Phi}_{RTIL}$ ($\bar{\Phi}_{CNT} = \bar{\Phi}_\sigma + \bar{\Phi}_{RTIL}$) and (c) specific capacitance of (*n*,*n*) nanotubes in $EMI^+BF_4^-$ at 1 atm and 350 K. Units: electric potential (V), specific capacitance (μF/cm²), σ_S (*e*/nm²), and d_0 (nm). The numbers in the legend of panel a denote the *n* values of the (*n*,*n*) armchair CNTs considered in the present study. In panel b, the contributions to the electrode potential from RTIL ions located in the interior of CNTs are plotted as open blue triangles. Except for the $n = 5$ case, the RTIL ions inside the nanotube account for more than ~80% of $\bar{\Phi}_{RTIL}$ (filled blue triangles). In panel c, open red squares and blue circles represent, respectively, positively and negatively charged electrodes, that is, anode and cathode, and filled black circles denote the total specific capacitance $\bar{c}_t$ in eq 4. (d) Comparison of the MD predictions for $\bar{c}_t$ with experimental results of ref 13. We scaled the experimental $\bar{c}_t$ values and their pore size by ~0.11 and ~1.3, respectively.

tion. To overcome this difficulty, we determine the electrode potential $\bar{\Phi}_{CNT}$ as the average of electric potential taken over all carbon and center-of-honeycomb sites of the CNT. While this approach may not be rigorous and thus poses a considerable limitation, it enables us to analyze capacitance systematically within our nonpolarizable nanotube description. Furthermore, key molecular aspects of supercapacitors needed to understand the influence of differing size and surface charge density of CNTs on RTIL structure relevant to capacitance are properly incorporated into our description. Thus a prudent view would be that while a proper account of electronic polarizability is needed for a quantitative analysis, our study here provides important insight into nanoporous supercapacitors at the qualitative and semiquantitative level in the molecular framework.

With the above caveat in mind, we consider the results for $\bar{\Phi}_{CNT}$ in Figure 2a. As expected, $\bar{\Phi}_{CNT}$ and CNT surface charge density σ_S have the same sign. Therefore the electric potential at the positively charged surface is positive as it should be and similarly for the negatively charged electrode. Hereafter, we will refer to the positively and negatively charged CNTs as the "anode" and "cathode", respectively. $\bar{\Phi}_{CNT}$ varies almost linearly with σ_S for most cases studied here (see below, however). For additional insight, we have decomposed $\bar{\Phi}_{CNT}$ into contributions from σ_S and RTIL ions, $\bar{\Phi}_{\sigma}$ and $\bar{\Phi}_{RTIL}$. The contribution from charges in the image cells needed in the Ewald method[30] is included in $\bar{\Phi}_{RTIL}$. The results obtained with $\sigma_S = 0.80-0.94$ e/nm^2 (see Table 1) are shown in Figure 2b as a function of the diameter d_0 of the (n,n) nanotube[24]

$$d_0 = \frac{3n}{\pi} l_{CC} \qquad (1)$$

where $l_{CC} = 0.1415$ nm is the carbon bond length.[31,32] Since $\bar{\Phi}_{\sigma}$ (filled squares) and $\bar{\Phi}_{RTIL}$ (filled triangles) are opposite in sign, the RTIL environment reduces the magnitude of the electrode potential compared to vacuo. We notice that the magnitudes of both $\bar{\Phi}_{\sigma}$ and $\bar{\Phi}_{RTIL}$ tend to increase with d_0. This trend is expected in that the total charge of the CNT increases with the nanotube size, that is, the diameter, for given σ_S. We nonetheless point out that the set of σ_S values employed in the simulations varied somewhat with individual CNTs to satisfy the overall electroneutrality condition of the CNT+RTIL system without introducing a background charge distribution. For details, see the Simulation Methods section. Therefore data points with different d_0 values in Figure 2b are characterized by somewhat different σ_S values. For instance, σ_S for $n = 7$ with $d_0 = 0.95$ nm is higher than that for $n = 8$ with $d_0 = 1.08$ nm by ~15% (see Table 1). This difference in σ_S is responsible for the nonmonotonic behavior of $\bar{\Phi}_{RTIL}$ near $d_0 = 1$ nm. Thus a direct comparison of data points at different d_0 needs caution. Despite this complication, we notice that the functional behavior of $\bar{\Phi}_{CNT}$ is dominated by $\bar{\Phi}_{RTIL}$ up to $d_0 \approx 1.1$ nm ($n = 8$), whereas it is mainly governed by $\bar{\Phi}_{\sigma}$ for larger pore size. This means that solvation *via* RTIL plays an important role in the electrode potential and thus in the capacitance for small micropores (see below). Though not shown here, we note that the electric potential in the bulk RTIL, determined as the potential at two end points of the "dumbbell" along the CNT axis in Figure 1 averaged over the MD trajectory, vanishes.

TABLE 1. Average Occupancy Numbers of Cations and Anions Inside (n,n) CNTs[a]

n	d_0	σ_S[b]	$N_i^{(+)}$	$N_i^{(-)}$	δ_{is}	$N^{(+)}$	$N^{(-)}$
5	0.68	0	0.0	0.0		340	340
		0.44 (4)	0.0	0.0	0	338	342
		0.88 (8)	0.0	0.0	0	336	344
		−0.44 (−4)	0.0	0.0	0	342	338
6	0.81	0	0.0	0.0		340	340
		0.55 (6)	0.0	4.0	0.94	336	342
		0.91 (10)	0.0	7.0	0.99	334	344
		−0.55 (−6)	2.1	0.0	0.49	342	336
7	0.95	0	0.03	0.0		340	340
		0.47 (6)	0.26	4.2	0.79	337	343
		0.94 (12)	0.0	9.0	0.90	334	346
		−0.47 (−6)	5.0	0.0	1.0	343	337
8	1.08	0	4.7	4.7		388	388
		0.41 (6)	2.3	6.0	0.65	384	390
		0.82 (12)	1.8	9.0	0.63	382	394
		−0.41 (−6)	5.0	0.0	0.88	390	384
10	1.35	0	12	12		488	488
		0.33 (6)	11	15	0.56	484	490
		0.82 (15)	7.7	19	0.64	481	496
		−0.33 (−6)	13	8.1	0.69	489	483
15	2.03	0	35	34		744	744
		0.40 (11)	32	39	0.36	738	749
		0.80 (22)	29	45	0.41	733	755
		−0.40 (−11)	37	29	0.41	747	736

[a] $N^{(\pm)}$ are the numbers of cations and anions employed in the simulations, δ_{is} is the relative strength of internal solvation in eq 3, and d_0 and σ_S are, respectively, the nanotube diameter in nm (eq 1) and surface charge density in units of e/nm^2, where e is the elementary charge. [b] Numbers in parentheses are the total charges of the CNTs measured in e.

We proceed to capacitance. The results for specific capacitance $\bar{c}$ normalized to the pore surface area

$$\bar{c} = \frac{\partial \sigma_S}{\partial \bar{\Phi}_{CNT}} \qquad (2)$$

for the anode and cathode at PZC (potential of zero charge) are exibited in Figure 2c. The most salient feature there is the nonmonotonic behavior of $\bar{c}$ with d_0. As the pore size decreases from $d_0 \approx 2$ nm to ~0.9 nm, $\bar{c}$ increases substantially for both electrodes. However, if we further reduce the CNT diameter, $\bar{c}$ begins to drop rapidly. Another noteworthy aspect is that the anodic

and cathodic $\bar{c}$ differ significantly for (6,6) and to a lesser extent for (7,7). This is a direct consequence of the deviation from the linear dependence of $\tilde{\Phi}_{CNT}$ on σ_S (*cf.* Figure 2a). (We will analyze the disparity between the anodic and cathodic capacitance of (6,6) in more detail below.) For all other CNTs that are either larger or smaller than (6,6) and (7,7), their respective anodic and cathodic specific capacitances are essentially the same. As a consequence, the maximum anodic $\bar{c}$ results at $d_0 = 0.81$ nm ($n = 6$), while the (7,7) micropore with $d_0 = 0.95$ nm yields the highest cathodic $\bar{c}$. In view of the results in Figure 2b above, $\tilde{\Phi}_{RTIL}$ is primarily responsible for the rapid rise and fall of $\bar{c}$ for $d_0 \lesssim 1.1$ nm, including the difference between the anode and cathode, while the gradual decline of $\bar{c}$ with the nanotube diameter for $d_0 \gtrsim 1.1$ nm is mainly due to $\tilde{\Phi}_{\sigma}$.

For better understanding of the $\bar{c}$ results, we consider "internal" RTIL ions, namely, ions present inside the nanotubes. We define the interior region of the (n,n) CNT as the cylindrical volume of diameter d_0 in eq 1 and height h given by the end-to-end, carbon-to-carbon distance. RTIL ions are assumed to be in the interior of the CNT if their center-of-mass is located inside the cylindrical volume thus defined.[23] MD results for the average numbers of internal cations and anions, termed occupancy numbers $N_i^{(\pm)}$, at 350 K are compiled in Table 1. Here and hereafter, superscripts (+) and (−) signify the cations and anions, respectively. Our results have several noteworthy features. First, there are no RTIL ions present inside the neutral (5,5), (6,6), and (7,7) CNTs. This indicates that the CNT micropores of diameters less than 1 nm are just too small to accommodate bulky EMI^+ and BF_4^- ions without the assistance of electrostatic interactions. Second, when charged, (6,6) allows only RTIL ions of opposite charge, that is, counterions, in its interior region. Thus internal solvation of (6,6) at equilibrium is effected exclusively *via* the counterions. The situation for (7,7) is very similar. Hereafter we will refer to solvation induced solely by a single ionic species or like-charge ions as "exclusive solvation". Because of their proximity to the pore surface, the internal counterions make a major contribution to $\tilde{\Phi}_{RTIL}$ that reduces the electrode potential. The results in Figure 2b show that they account for about 90% of $\tilde{\Phi}_{RTIL}$ in the case of (6,6) and (7,7) which have only counterions as internal ions ("exclusive internal solvation"). This indicates that the internal counterions play a crucial role in increasing $\bar{c}$ (*cf.* eq 2). We thus expect that the specific capacitance of (6,6) and (7,7) is considerably enhanced in $EMI^+BF_4^-$. By contrast, the (5,5) tunnel is too narrow to allow internal RTIL ions even with the aid of strong CNT-RTIL electrostatic interactions. This results in much weaker $\tilde{\Phi}_{RTIL}$ (see Figure 2b) and thus substantially lower $\bar{c}$ for (5,5) than for (6,6) and (7,7).

For larger (8,8), (10,10), and (15,15) CNTs, both EMI^+ and BF_4^- ions are present inside the pore regardless of σ_S with one exception. As the occupancy numbers of internal co-ions and counterions increase with the CNT size, the extent of cancellation of their opposing effects on the electrode potential, that is, enhancement *via* co-ions *versus* reduction *via* counterions of $\tilde{\Phi}_{CNT}$, will grow accordingly. We therefore expect a relatively minor role for $\tilde{\Phi}_{RTIL}$ and thus a dominant role for $\tilde{\Phi}_{\sigma}$ for these CNTs, compared to (6,6) and (7,7) characterized by exclusive internal solvation. To see this better, we introduce δ_{is}

$$\delta_{is} = k_{is}\frac{\Delta N_i}{d_0 Q}; \qquad \Delta N_i \equiv |N_i^{(+)} - N_i^{(-)}| \tag{3}$$

where Q is the magnitude of the total charge of the electrode and k_{is} is a proportionality constant. We note that δ_{is} gauges the average stabilization of nanotubes, induced by internal RTIL ions, normalized to the CNT charge, and thus measures the relative strength of internal solvation, compared with Φ_{σ}. For convenience, we choose $k_{is} = 1.14e$ nm, so that δ_{is} is dimensionless and its value for the (7,7) CNT with $\sigma_S = -0.47$ e/nm^2 is unity. The δ_{is} results in Table 1 confirm that the internal RTIL ions play a progressively minor role as the CNT size grows. This is responsible for the transition from the strong to weak size-dependence of $\bar{c}$ with increasing d_0 in Figure 2c. It is worthwhile to note from Figure 2b that despite their diminishing role in $\bar{c}$ modulations, the internal RTIL ions are still the main contributor to $\tilde{\Phi}_{RTIL}$ for $n = 8-15$, analogous to the (6,6) and (7,7) cases.

In Figure 2d, the overall specific capacitance $\bar{c}_t$ of the cathode−anode supercapacitor system

$$1/\bar{c}_t = 1/\bar{c}\ (\text{anode}) + 1/\bar{c}\ (\text{cathode}) \tag{4}$$

is shown as a function of d_0. For comparison, the experimental results of ref 13 are also displayed there. We scaled the $\bar{c}_t$ values and pore size there by ~0.11 and by ~1.3, respectively, so that the resulting height and position of the $\bar{c}_t$ maximum coincide with the MD predictions. It should be noted that the estimation of pore size in ref 13 was based on slit geometry, which is rather different from nanotube tunnels employed here. Except for its overall magnitude, the detailed trend of $\bar{c}_t$ with pore size is well reproduced by simulations. Considering the approximations and simplifications invoked in MD, this level of agreement with the experiments is quite impressive.

For perspective, we consider here potential factors that would be responsible for the discrepancy in the $\bar{c}_t$ magnitude between the simulations and experiments. The first and foremost is the complete neglect of electronic polarizability for both the CNTs and RTIL in our model description. Its inclusion would enhance the surface charge on the CNTs and molecular dipole moments of the RTIL ions, both *via* induced charges. This would in turn increase the electric field strength inside the pore and thus the stored energy, thereby raising the specific capacitance significantly. For instance, account-

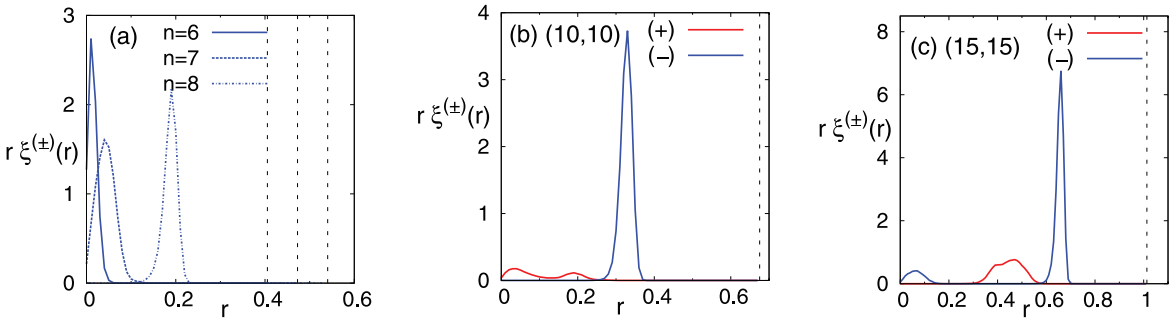

Figure 3. Results for $r\xi^{(\pm)}(r)$ of EMI^+ and BF_4^- ions inside of CNT anodes charged with $\sigma_S = 0.80-0.94$ e/nm^2 (Table 1). In panel a, only the results for $r\xi^{(-)}(r)$ are displayed; r is the distance (units: nm) in the radial direction from the nanotube axis and dashed vertical lines denote the position of the CNT wall. Representative snapshots of internal RTIL ions are presented in Figure 4.

ing for RTIL polarizability alone in the dielectric continuum context would increase the MD predictions for $\bar{c}_t$ by at least a factor of ~2 (see below). Second, the difference in pore geometry between the simulation and experimental systems could also play a non-negligible role. To be specific, nanotube tunnels employed in the present study may not be optimal for specific capacitance. Other geometry such as slits which would be closer to the real shapes of micropores could be more efficient and thus yield higher $\bar{c}$. Third, potential uncertainties in the estimation of the pore surface area of activated carbon materials could also contribute to the quantitative difference in $\bar{c}_t$ between the simulation and experiments.

Returning to our main thread, we examine distributions of RTIL ions inside the micropores to obtain a more detailed molecular picture of CNT supercapacitors. We use the cylindrical coordinate system (r,ϕ,z), where the center of the CNT under consideration is at the origin, its axis lies in the z direction, and r is the radial distance measured from the z-axis. We consider the number of cations and anions, $N^{(\pm)}(r,z)$, inside a cylindrical volume, extending from $-z$ to z with a base circle of radius r. $N^{(\pm)}(r,z)$ is related to local number densities $n^{(\pm)}(r,\phi,z)$ of cations and anions *via*

$$N^{(\pm)}(r,z) = \int_0^r \int_0^{2\pi} \int_{-z}^{z} r'\,dr'\,d\phi'\,dz'^{(\pm)}(r',\phi',z') \tag{5}$$

where the center-of-mass is used to represent the positions of individual ions. We point out that $N_i^{(\pm)}$ in Table 1 is related to $N^{(\pm)}(r,z)$ *via* $N_i^{(\pm)} = N^{(\pm)}(d_0/2,h/2)$. Following our prior study,[23] we define the dimensionless radial distributions of ions as

$$\xi^{(\pm)}(r) = (2\pi n_0^{(\pm)} rh)^{-1} \frac{\partial}{\partial r} N^{(\pm)}(r,h/2) \tag{6}$$

where $n_0^{(\pm)}$ are the cation and anion number densities in the bulk. $\xi^{(\pm)}(r)$ in eq 6 gauges variations of probability distributions of internal ions as the distance r from the nanotube axis increases.

Figure 3 shows MD results for $r\xi^{(\pm)}(r)$ with $\sigma_S = 0.80-0.94$ e/nm^2. For additional insight, representative snapshots of the center-of-mass positions of internal ions are displayed in Figure 4. One of the most prominent features is that $\xi^{(\pm)}(r)$ varies significantly with the nanotube size. The $n = 5$ case is characterized by $r\xi^{(\pm)}(r) = 0$ because $N_i^{(\pm)} = 0$. For $n = 6$ and 7 (0.8 nm $\lesssim d_0 \lesssim$ 1 nm), only counterions show a nonvanishing radial distribution inside the CNTs as expected from their $N_i^{(\pm)}$ results, that is, exclusive internal solvation. The (8,8) case is similar to $n = 6$ and 7 in that the amplitude of its $r\xi^{(\pm)}(r)$ for internal co-ions (not shown) is small (*cf.* Table 1). The internal counterions for $n = 6-8$ exhibit a narrow single-peak distribution, indicating that they form on average a monolayer structure in the radial direction inside of the micropores. Their peak position shifts outward with growing d_0 and the corresponding solvation structure changes from a well-defined single-file distribution near the nanotube axis for $n = 6$ (Figure 4a) to a more zigzag structure for $n = 8$ (Figure 4b). As we further increase the CNT size to $d_0 = 1.35$ nm ($n = 10$), a discernible co-ion structure appears inside the internal solvation shell of counterions. The distribution of the co-ions is considerably broader than that of the counterions (*cf.* Figure 4c). The internal RTIL structure of (10,10) is thus characterized by a zigzag co-ion layer, surrounded by a cylindrical counterion shell near the CNT interior wall. For (15,15) with $d_0 = 2.03$ nm, the pore size is large enough to allow three internal solvation shells. Specifically, a weak single-file structure of counterions near the center of the CNT micropore is surrounded by the secondary co-ion layer, which is located inside of the primary counterion shell. Though not presented here, the RTIL distributions inside of negatively charged CNTs generally show a similar dependence on the pore size. A notable exception is the (6,6) CNT, which shows a pronounced disparity between its anodic and cathodic capacitance as observed in Figure 2c above. We consider this next.

According to the MD results in Table 1, the cation occupancy number ($N_i^{(+)} = 2.1$) for the (6,6) cathode with $\sigma_S = -0.55e$/nm^2 is considerably smaller than the corresponding anode value $N_i^{(-)} = 4$. The situation for δ_{is} is very similar (0.49 *vs* 0.94). This difference in $N_i^{(\pm)}$ and δ_{is} between the $n = 6$ cathode and anode is ascribed to the size difference between EMI^+ and BF_4^-. If we assume

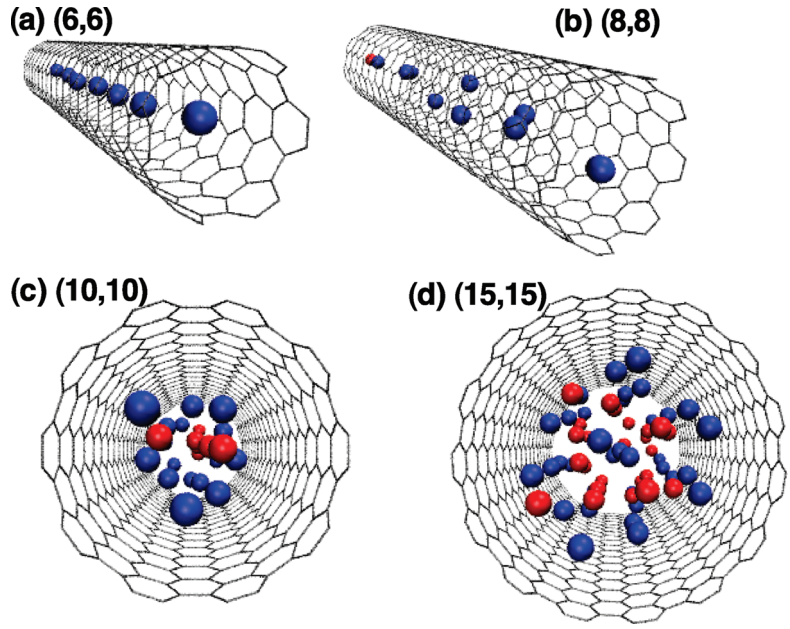

Figure 4. Snapshots of internal RTIL ions associated with the radial distributions inside the CNT anodes in Figure 3. Red and blue dots represent the center-of-mass positions of EMI^+ and BF_4^- ions, respectively.

that each constituent atom of RTIL is a sphere whose diameter is given by its Lennard-Jones σ parameter,[27−29] we estimate that the respective diameters of cross sections of EMI^+ and BF_4^- perpendicular to their major axes are ~0.67 and ~0.56 nm. Since the value of the σ parameter employed for CNT carbon atoms is 0.34 nm,[32] larger EMI^+ ions will not enter the narrow (6,6) pore of $d_0 = 0.81$ nm as well as smaller BF_4^-. For a clear exposition of this, the anion and cation radial distributions inside the (6,6) electrode with $\sigma_S = \pm 0.55e/nm^2$ are compared in Figure 5. Snapshots of internal ion configurations in the space-filling representation are also presented there for further illustration. We notice that $r\xi^{(+)}(r)$ for EMI^+ ions is considerably narrower than $r\xi^{(-)}(r)$ for BF_4^-. Furthermore, the maximum of the former distribution is located at $r = 0$, whereas the peak position of the latter is somewhat off-center from the nanotube axis. This indicates that the radial dimension of the (6,6) cathode is very tight for large EMI^+ ions, so that they barely fit into its tunnel. Relatively small BF_4^- ions, on the other hand, have more room inside the (6,6) micropore and thus are characterized by larger structural fluctuations along r than are the bulky EMI^+ ions. As a consequence, the number of EMI^+ ions inside the (6,6) cathode is smaller than that of BF_4^- inside its anodic counterpart by a factor of 2. Because the internal counterions tend to enhance specific capacitance, the cathodic $\bar{c}$ for (6,6) is considerably lower than its anodic value (Figure 2c).

A snapshot of internal RTIL ions inside the (7,7) nanotube with $\sigma_S = -0.47\ e/nm^2$ is exhibited in Figure 5d. Its comparison with Figure 5c exposes a dramatic enhancement in the cation occupancy of the cathode as the size of the micropore grows. To be specific, a mere 0.14 nm increase in the pore diameter leads to a marked rise in $N_i^{(+)}$ even though the Coulombic attraction between the CNT and EMI^+ becomes weakened due to a decrease in $|\sigma_S|$. This illustrates the strong influence

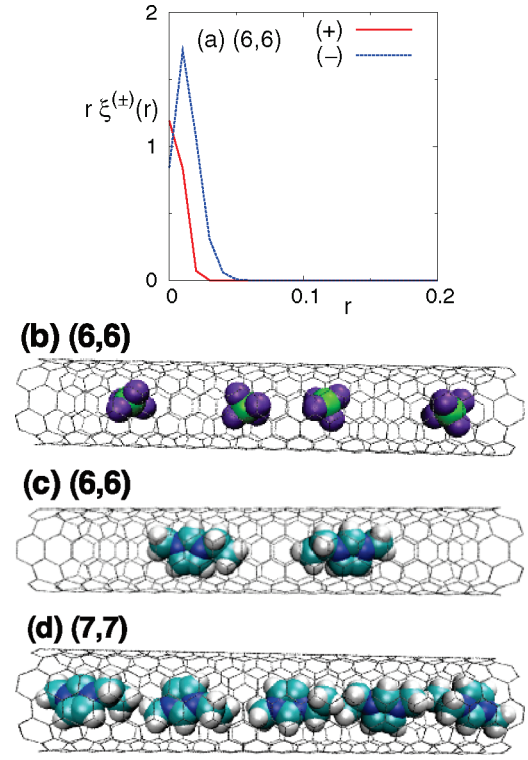

Figure 5. (a) Radial distributions of the internal anions (blue) and cations (red) of the (6,6) anode and cathode, respectively. The nanotube surface charge densities are $\sigma_S = \pm 0.55e/nm^2$. Because of exclusive internal solvation, only cations (anions) are present inside the cathode (anode). Snapshots of the internal RTIL ions inside the (b) anodic and (c) cathodic (6,6) nanotubes. σ_S is the same as in panel a. (d) Snapshot of internal RTIL ions of the (7,7) cathode with $\sigma_S = -0.47e/nm^2$.

through steric hindrance the nanotube size can exert on the internal RTIL structure and thus specific capacitance. However, it should also be pointed out that a similar size increase has little impact on the anion occupancy of the corresponding anode (see Table 1), revealing its striking difference from the cathode. This cathode−anode asymmetry[20] is another manifestation of the cation−anion size difference considered above. One important consequence of this asymmetry is the difference in the extent of exclusive internal solvation between the cathode and anode. As one can easily guess from the two EMI^+ configurations in Figure 5, exclusive solvation for the (6,6) cathode is not as extensive as that for the (7,7) cathode; their respective δ_{is} values are 0.49 and 1 (Table 1). By contrast, the strength of exclusive solvation for the anodes is higher for $n = 6$ ($\delta_{is} = 0.94$) than for $n = 7$ ($\delta_{is} = 0.79$). This difference explains the differing $\bar{c}$ behavior between the cathode and anode in Figure 2c, that is, cathodic $\bar{c}$ drops abruptly from its maximum at $n = 7$ with $d_0 = 0.95$ nm as the nanotube size decreases, whereas anodic $\bar{c}$ peaks at smaller $d_0 = 0.81$ nm, corresponding to (6,6). This also suggests that the highest $\bar{c}$ value results when exclusive solvation of the electrode *via* internal counterions is maximized. Using the estimates of ion size above, we deduce that maximal exclusive solvation occurs when the ion diameter is smaller than the pore diameter d_0 by ~0.3 nm, corresponding to the size of nanotube C atoms. In view of differing definitions of pore size, that is, whether or not the carbon size is reflected in d_0, our finding here seems to confirm the conjecture that $\bar{c}$ is maximized when the ion size is comparable to the pore size.[13,15,21,22]

We turn to the local charge density $\rho(r,z,\phi)$ arising from the internal ions. For convenience, we average ρ over ϕ to eliminate its angle dependence

$$\bar{\rho}(r,z) \equiv \frac{1}{2\pi}\int_0^{2\pi} d\phi\, \rho(r,z,\phi) \qquad (7)$$

The results for $r\bar{\rho}(r,z)$ inside the CNT anodes with $\sigma_S = 0.80-0.94$ e/nm^2 are shown in Figure 6. As expected, $r\bar{\rho}(r,z)$ varies substantially with the size of the micropore. One remarkable aspect is that the charge distribution for $n = 6-8$ shows two distinct layers of opposite charges. Since the (6,6) and (7,7) CNTs (and also (8,8) to a large extent) are characterized by a monolayer solvation structure consisting of only counterions, which are BF_4^- anions in the present $\sigma_S > 0$ case, the existence of ("red") regions of excess positive charges is counterintuitive in Figure 6a−c. This intriguing feature is not limited to the positive σ_S case. The charge density inside of, for instance, the (7,7) cathode with $\sigma_S = -0.47e$/nm^2 in Figure 7a shows a similar behavior. Even though the micropore is occupied solely by in this case EMI^+ ions, corresponding $\bar{\rho}(r,z)$ exhibits multiple layers with alternating signs. We attribute this unexpected result of $\bar{\rho}(r,z)$ to the extended nature of RTIL ion charge distributions. Specifically, F and B atoms of anions have, respectively, partial negative (−0.5376e) and positive (1.1504e) charges, which lead to charge separation through preferential orientation[19] near the electrified CNT wall and analogously for EMI^+ cations. Therefore, even though co-ions are completely absent and only one layer of counterions is present, there exist in effect multiple shells of alternating charges inside the micropore. We believe that this interesting property is unique to molecular ions with extended charge distributions. Atomic ions, for example, Cl^-, will not show

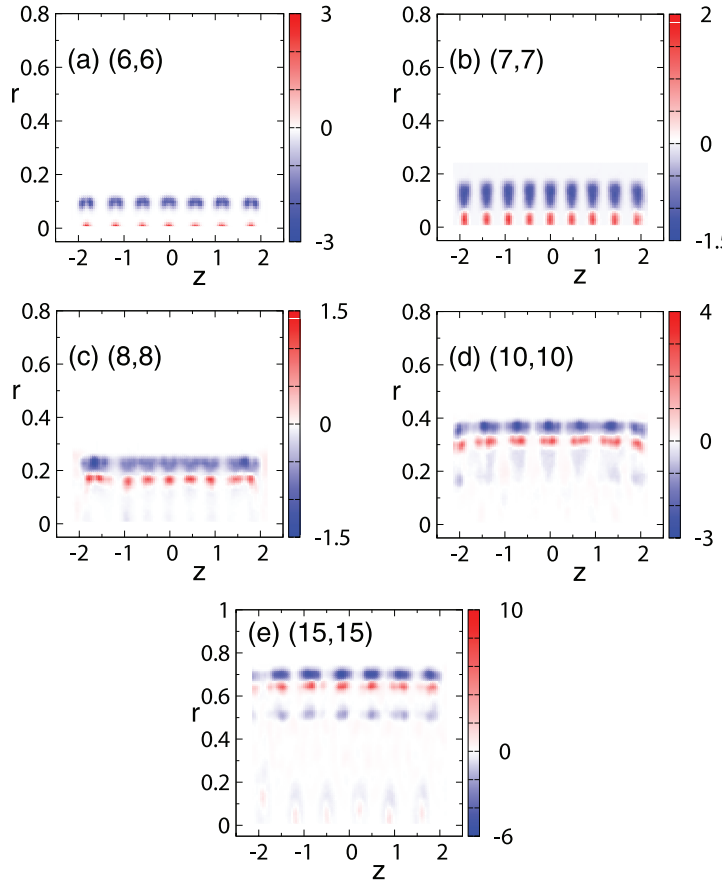

Figure 6. Charge density of RTIL ions inside the CNT anodes. The results for $r\bar{\rho}(r,z)$ are plotted, where $r\bar{\rho}$ is in units of e/nm^2 and r and z are measured in nm. The vertical bar in each panel shows the color scale employed to quantify $r\bar{\rho}(r,z)$. The nanotube surface charge density is the same as in Figures 3 and 4.

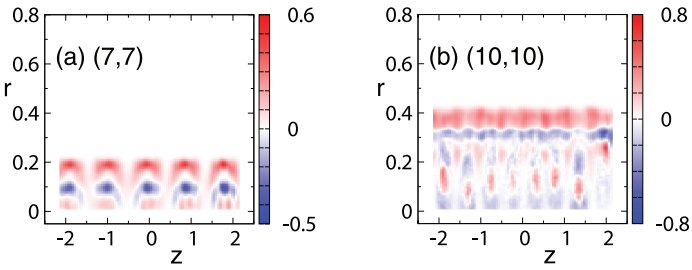

Figure 7. MD results for $r\bar{\rho}(r,z)$ inside the CNT cathodes with $\sigma_S \approx -0.4e$/nm^2 (Table 1). For brevity, only the $n = 7$ and 10 cases are presented.

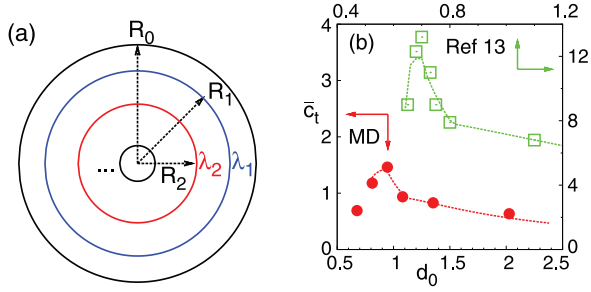

Figure 8. (a) EMLC model; (b) MD and experimental[13] results for $\bar{c}_t$ (units: μF/cm²) and their fits *via* EMLC. The fits are shown in dotted lines.

this behavior although we do not completely exclude the possibility that large ions, such as I^-, could yield a similar effect but to a much lesser degree through induced polarization.

The (10,10) and (15,15) CNTs, which have both EMI^+ and BF_4^- as the internal ions, are characterized by more layers in $r\bar{\rho}(r,z)$ than (6,6)−(8,8). Though not as pronounced as counterions, we note that the co-ions also yield charge densities with alternating signs (not shown here). Our results here strongly indicate that the so-called "compact layer"[1] of EDLCs is actually composed of multiple layers of alternating charges partly due to the extended charge distribution of RTIL ions and partly due to the presence of ions of opposite charges. The charge distribution of the compact layer is not symmetric[20] about the PZC because of the complete lack of symmetry in molecular structure between EMI^+ and BF_4^- (*cf.* Figure 6b *vs* Figure 7a).

Finally we consider a model description that can be used to understand the capacitance behavior of CNT supercapacitors in RTILs. In view of the MD results in Figures 6 and 7, we propose an electric multiple-charge layer capacitor (EMLC) model (Figure 8a), where we assume that there are n layers of concentric cylindrical charge distributions inside the micropore of infinite length and the electric field vanishes both outside of the CNT wall and inside of the innermost charge layer. For convenience, the charge layers are numbered in the order of the decreasing diameter, starting with the CNT interior wall as the $i = 0$ layer. The electric field $E_r^{(i)}$ and displacement vector $D_r^{(i)}$ along the radial direction in the region between two layers $i - 1$ and i are

$$D_r^{(i)} = \frac{2\Lambda_i}{r}; \quad E_r^{(i)} = \frac{2\Lambda_i}{\varepsilon r}; \quad \Lambda_i = \sum_{j=i}^{n} \lambda_j; \quad \lambda_i \equiv 2\pi R_i \sigma_i \tag{8}$$

where ε is the medium dielectric constant, R_i is the radius of the layer i, σ_i and λ_i are, respectively, the surface charge density and corresponding line charge density of i, and Λ_i is the sum of the line charge densities over the layers i through n. The energy stored in this EMLC model system of length dz is given by

$$\frac{1}{2}\frac{(dq)^2}{dC} = \frac{1}{2}\frac{(\lambda_0 dz)^2}{2\pi R_0 \bar{c} dz} = \frac{1}{8\pi} dz \sum_{j=1}^{n} \int_{R_i}^{R_{i-1}} dr\, 2\pi r E_r^{(i)} D_r^{(i)}$$
$$= \frac{1}{\varepsilon} dz \sum_{j=1}^{n} \Lambda_i^2 \ln(R_{i-1}/R_i) \tag{9}$$

where dq and dC are the charge and capacitance of the EMLC. We thus deduce

$$\bar{c} = \varepsilon[4\pi R_0 \sum_{j=1}^{n} (\Lambda_i^2/\lambda_0^2) \ln(R_{i-1}/R_i)]^{-1} \tag{10}$$

Because of our assumption that $E_r = D_r = 0$ outside of the CNT (*viz.*, $r > R_0$), the net charge of EMLC, that is, the sum of the charges of the pore surface and n cylindrical layers, $\lambda_0 + \sum_{i=1}^{n}\lambda_i$, vanishes. This yields $\Lambda_1(= \sum_{i=1}^{n}\lambda_i) = -\lambda_0$, so that eq 10 becomes

$$\bar{c} = \varepsilon/(4\pi R_0[\ln(R_0/R_1) + (\Lambda_2^2/\lambda_0^2) \ln(R_1/R_2) + \cdots$$
$$+ (\Lambda_n^2/\lambda_0^2) \ln(R_{n-1}/R_n)]) \tag{11}$$

It should be pointed out that EMLC consisting of infinitely long and concentric charge distributions is different from the CNT micropores of finite length because ions not only in the interior of nanotubes but also in the bulk RTIL contribute to capacitance of the latter. However, since the internal RTIL ions play a much more important role than those in the bulk as observed in Figure 2b above, we believe that EMLC offers an intuitive model framework to understand and interpret the MD and experimental results, including their differences (see below). Indeed, similar but simpler electric wire-in-cylinder and electric double-cylinder model descriptions proposed by Huang *et al.*[21,22] have provided interesting insight into capacitance of nanoporous systems. It is also worthy of note that the EMLC theory in eq 11 goes beyond these earlier models[21,22] in two important ways. First, our description takes into account the charge separation of the primary counterion shell (and other secondary shells) arising from the extended nature of RTIL ion charge distributions. Second, it also reflects properly the multilayered aspect of the charge distribution in the compact layer. Note that $\varepsilon = 1$ for our supercapacitor systems because the RTIL electronic polarizability is neglected in the simulations. If it would be incorporated in the framework of the dielectric continuum description, specifically, optical dielectric constant ε_∞, we estimate with the aid of measurements[33−35] of the index of refraction n_r that $\varepsilon_\infty = n_r^2 \approx 2$, although considerably different (and often higher) ε_∞ values[36−39] have also been reported. All things being equal, this would result in at least a 2-fold increase in the $\bar{c}$ predictions. We also note that accounting for of the nonlinear polarizability[40] and extended character, that is, higher multipole moments,[41] of induced charge distributions could lead to further enhancement of $\bar{c}$ over and

TABLE 2. Fitting Parameters for EMLC[a]

EMLC[b]		ε	R_1	R_2	R_3	Λ_2/λ_0	Λ_3/λ_0
MD (+)	$n = 2$	1	$R_0 - 0.2$	0.12		0.4	
	$n = 2$		$R_0 - 0.25$	0.24		1.1	
	$n = 3$		$R_0 - 0.25$	$R_0 - 0.37$	0.26	0.89	0.60
MD (−)	$n = 2$		$R_0 - 0.15$	$R_0 - 0.38$		0.45	
	$n = 2$		$R_0 - 0.23$	0.25		1.1	
	$n = 3$		$R_0 - 0.25$	$R_0 - 0.37$	0.26	0.89	0.60
exptl (+)	$n = 2$	2	$R_0 - 0.05$	0.25		0.67	
	$n = 3$		$R_0 - 0.09$	$R_0 - 0.15$	0.27	0.4	0.3
exptl (−)	$n = 2$		$R_0 - 0.02$	$R_0 - 0.32$		0.23	
	$n = 2$		$R_0 - 0.05$	0.282		0.8	
	$n = 3$		$R_0 - 0.09$	$R_0 - 0.15$	0.27	0.4	0.3

[a]MD and exptl denote the MD results presented here and experimental data from ref 13: anode (+); cathode (−). [b]The first and second of two different $n = 2$ parameter sets describe, respectively, the rapid rise and fall of $\bar{c}_t$ with increasing d_0, while $n = 3$ models its gradual decline.

above the estimation based on the dielectric continuum description, especially in a nanoenvironment where molecularity would play an important role.

We fitted both the experimental[13,15] and simulation results using eq 11. For the latter, we fitted the cathodic and anodic $\bar{c}$ separately. As for the former, in the absence of experimental information on single electrode capacitance, we assumed that the anodic and cathodic capacitances differ in the region $d_0 \lesssim$ 0.8 nm, where $\bar{c}$ varies rapidly with the pore size, and their relative differences are similar to the MD results. The fitting parameters and results are presented in Table 2 and Figure 8b, respectively. Good agreement between the data and their fits suggests that eq 11 based on the compact layer comprising multiple charge layers provides a reasonable theoretical framework to understand capacitance of nanoporous EDLCs in RTILs. A couple of points are worth mentioning here. First, we employed two different regimes of EMLC, namely, $n = 2$ and 3 in Table 2, to fit the part of the data, which shows a decreasing $\bar{c}_t$ trend with increasing d_0 because a single EMLC regime with one n did not yield a good fit. This appears to provide indirect evidence that the compact layer structure and associated charge distributions vary considerably with the micropore size. Second, the $i = 1$ charge layer is located closer to the electrode surface in the fits to the measurements than those to MD. This seems to imply that because of the diffuse character of electron density of the electrodes and RTIL ions (which becomes further polarized in the presence of opposite charges), the actual charge-to-charge separation between the electrodes and counterions in the double layer would be considerably shorter than the predictions of the force-field descriptions couched in point charges situated at atom centers.[25] This is another reason why MD underestimates $\bar{c}_t$ compared to experiments.

CONCLUDING REMARKS

We have studied the capacitance of a carbon nanotube micropore in $EMI^+BF_4^-$ as a function of its diameter in the range 0.7 nm $\lesssim d_0 \lesssim$ 2 nm using MD simulations. The specific capacitance $\bar{c}$ normalized to the pore surface area was found to vary significantly with d_0 in a nonmonotonic manner. For 0.9 nm $\lesssim d_0 \lesssim$ 2 nm, $\bar{c}$ increases with decreasing d_0. One of the main factors responsible for this behavior is the growing difference of internal solvation *via* counterions and *via* co-ions and thus the progressively more important role internal counterions play as the micropore becomes smaller in diameter. As d_0 further reduces below ~0.8 nm, however, $\bar{c}$ begins to drop rapidly. This was attributed to a rapid transition from strong exclusive internal solvation to the complete lack of internal solvation for very small CNTs. Our results for the detailed trend of the specific capacitance with d_0 are in excellent accord with the recent measurements[13,15] of EDLCs based on carbide-derived carbon materials. Nevertheless, the MD predictions for the overall magnitude of specific capacitance show a significant departure from the experiments. Possible reasons for this discrepancy include the neglect of electronic polarizability and absence of diffuse character of electron density and related spillover density in the simulations, potential uncertainties in the determination of pore area in the measurements and the difference in pore geometry between MD and experiments.

We analyzed the structure and charge distribution of the internal compact layer of CNT supercapacitors. For (6,6) and (7,7), nearly all of the internal ions are counterions, which form essentially a single-file distribution. Interestingly, these counterions yield a charge density of multiple layers with alternating signs even though all ions have exactly the same charge. This surprising result is attributed to orientational alignment of bulky ions with extended charge distributions inside the electrified CNTs. The (8,8) shows similar characteristics. As the nanotube size increases, both the counterions and co-ions develop alternating shell-like structures. For (10,10), a co-ion distribution near the center of the CNT is surrounded by a counterion shell near its interior wall. In the case of (15,15), the largest CNT we studied, three internal solvation layers that alternate between counterions and co-ions result. The (5,5) CNT on the other hand was found to be too small to allow internal RTIL ions regardless of its surface charge density.

We found that the highest single-electrode specific capacitance is obtained when internal solvation is effected maximally and exclusively *via* counterions, namely, a maximum number of RTIL counterions form a single-file distribution inside the CNT. Our analysis indicates that maximum exclusive solvation occurs when the diameter of counterions is comparable to the pore diameter minus the CNT carbon diameter. Since EMI^+

and BF_4^- ions differ in size, so do the cathode and anode that show maximal exclusive solvation and thus highest $\bar{c}$. To be specific, the (7,7) CNT with $d_0 = 0.95$ nm results in maximum cathodic $\bar{c}$, while anodic $\bar{c}$ reaches its maximum at $d_0 = 0.81$ nm corresponding to the (6,6) nanotube. This suggests that for a given RTIL, one can in principle maximize the specific capacitance of EDLCs by optimizing the anode and cathode pore size separately.

For the sake of efficient simulations, electronic polarizability of the CNT and RTIL was not incorporated in the present work. One shortcoming of this simplification is a significant underestimation of $\bar{c}$. A quick estimation using, for instance, the EMLC model indicates that the inclusion of RTIL polarizability[26] alone would increase the magnitude of $\bar{c}$ by a factor of at least ~2. It would thus be worthwhile in the future to lift this restriction and examine the electronic effects, including those of electrodes,[25] on the capacitance of micropores. It would also be desirable to go beyond CNTs and study other EDLC systems such as slit-geometry carbon micropores and graphene-based supercapacitors[42] in RTILs. This will help to understand how the electrode geometry influences capacitance and its power efficiency at the molecular level. Another important topic not studied here that has a direct bearing on power density of EDLCs is RTIL transport behavior inside the pores. To address this issue, we are currently investigating RTIL conductivity[43] inside electrified nanotubes. Finally, it would be extremely worthwhile to extend our study by employing an approach similar to, for example, electron transfer simulations,[44−47] to analyze pseudocapacitance.[2,48]

SIMULATION METHODS

A carbon-based micropore was modeled as a rigid and uniformly charged, single-walled CNT with carbon bond length $l_{CC} = 0.1415$ nm,[31,32] surrounded by a disk-shaped structureless slab that repels solvents. The length h of the CNT and the thickness of the slab were both 4.3 nm. Either side of the slab interfaces with bulk RTIL composed of EMI^+ and BF_4^- ions, which are allowed to enter the CNT tunnel. Six different nanotubes in the armchair configuration, (5,5), (6,6), (7,7), (8,8), (10,10) and (15,15), were studied. For each CNT, four different charge assignments were considered for C atoms, such that the resulting surface charge densities were either neutral or close to $0.8e/nm^2$ or $\pm 0.4e/nm^2$. We adjusted σ_S, so that the individual CNTs have integral charges when measured in units of e. This was needed to meet the charge neutrality of the entire simulation system by adjusting the numbers of RTIL cations and anions, $N^{(+)}$ and $N^{(-)}$ (see Table 1). In other words, for each case, σ_S, $N^{(+)}$ and $N^{(-)}$ were chosen so that the total charge of the electrified CNT and RTIL ions in the simulation cell vanishes without the introduction of background charges. We employed the same Lennard-Jones parameters[32] as in our prior work[23] for the nanotube C atoms. The only difference in the CNT description from ref 23 was that two ends of nanotubes were not terminated with H atoms in the present study. As for RTIL, the flexible all-atom potential models of refs 27 and 28 and of ref 29 were used for EMI^+ and BF_4^-, respectively. For interactions with the slab, we used the Lennard-Jones-type potential, the parameters of which were determined by fitting the interactions of each atom type of RTIL with a flat nanotube wall of infinite size, namely a graphene sheet (for details, see Table 3).

MD simulations were performed in the canonical ensemble[49,50] at 350 K using the DL_POLY program.[51] The EDLC system, micropore+RTIL, was restricted in the radial direction to the volume inside of a large nanotube to reduce the system size and increase the efficiency of simulations. Specifically, the (31,31) nanotube tunnel was employed to radially confine supercapacitors with $n = 5$, 6, and 7 micropores. For $n = 8$, 10, and 15 micropores, we used (33,33), (36,36), and (43,43), respectively. The EDLC system thus confined was placed in an orthorhombic cell of dimension $30.0 \times 30.0 \times 12.8$ nm^3 with the CNT micropore at the center of the cell. Therefore the volume occupied by RTIL in the central simulation cell takes the shape of a dumbbell (Figure 1). The resulting RTIL density outside of the micropore was close to the bulk value $n_0^{(\pm)} = 3.7$ nm^{-3}, obtained in separate simulations of neat $EMI^+BF_4^-$ in the *NPT* ensemble at 350 K and 1 atm. All CNT carbon and RTIL charges were held fixed (*i.e.*, nonpolarizable) during the simulations. The long-range electrostatic interactions and electric potentials were computed *via* the standard Ewald method,[30] using periodic orthorhombic boundary conditions. The trajectories were integrated *via* the Verlet leapfrog algorithm using a time step of 1 fs. Simulations in the canonical ensemble were carried out with 3 ns of equilibration, followed by a 2 ns trajectory from which averages were computed.

TABLE 3. Interaction Parameters for Slab[a]

atom	A_s (kcal/mol)	B_s (kcal/mol)	z_0 (nm)
N	2.2	3.1	0.315
C	1.5	2.1	0.33
H	0.50	0.75	0.28
B	1.2	2.0	0.34
F	1.2	1.8	0.31

[a] Atom−slab interaction is modeled as $U(z) = A_s(z_0/z)^{12} - B_s(z_0/z)^6$, where z is the distance between the atom and slab surface. A_s, B_s, and z_0 for each atom type of RTIL were determined by fitting each of their interactions with an infinite carbon wall (*i.e.*, graphene sheet).

Acknowledgment. This research was supported in part by the National Science Foundation through TeraGrid resources provided by Pittsburgh Supercomputing Center.

REFERENCES AND NOTES

1. Parsons, R. Electrical Double Layer: Recent Experimental and Theoretical Developments. *Chem. Rev.* **1990**, *90*, 813–826.
2. Conway, B. E. *Electrochemical Supercapacitors: Scientific Fundamentals and Technological Applications*; Plenum: New York, 1999.
3. Kötz, R.; Carlen, M. Principles and Applications of Electrochemical Capacitors. *Electrochim. Acta* **2000**, *45*, 2483–2498.
4. Pandolfo, A. G.; Hollenkamp, A. F. Carbon Properties and Their Role in Supercapacitors. *J. Power Sources* **2006**, *157*, 11–27.
5. Frackowiak, E. Carbon Materials for Supercapacitor Application. *Phys. Chem. Chem. Phys.* **2007**, *9*, 1774–1785.
6. Nanjundiah, C.; McDevitt, S. F.; Koch, V. R. Differential Capacitance Measurements in Solvent-Free Ionic Liquids at Hg and C Interfaces. *J. Electrochem. Soc.* **1997**, *144*, 3392–3397.
7. Ue, M.; Takeda, M.; Toriumi, A.; Kominato, A.; Hagiwara, R.; Ito, Y. Application of Low-Viscosity Ionic Liquid to the Electrolyte of Double-Layer Capacitors. *J. Electrochem. Soc.* **2003**, *150*, A499–A502.

8. Ue, M. Application of Ionic Liquid to Double-Layer Capacitors. In *Electrochemical Aspects of Ionic Liquids*; Ohno, H., Ed.; John Wiley & Sons: Hoboken, NJ, 2005; Chapter 17.
9. Lewandowski, A.; Galiński, M. Carbon−Ionic Liquid Double Layer Capacitors. *J. Phys. Chem. Sol.* **2004**, *65*, 281–286.
10. Frackowiak, E.; Lota, G.; Pernak, J. Room-Temperature Phosphonium Ionic Liquids for Supercapacitor Application. *Appl. Phys. Lett.* **2005**, *86*, 164194.
11. Raymundo-Pinero, E.; Kierzek, K.; Machnikowski, J.; Béguin, F. Relationship between the Nanoporous Texture of Activated Carbons and Their Capacitance Properties in Different Electrolytes. *Carbon* **2006**, *44*, 2498–2507.
12. Chmiola, J.; Yushin, G.; Gogotsi, Y.; Portet, C.; Simon, P.; Taberna, P. L. Anomalous Increase in Carbon Capacitance at Pore Sizes Less than 1 Nanometer. *Science* **2006**, *313*, 1760–1763.
13. Largeot, C.; Portet, C.; Chmiola, J.; Taberna, P. L.; Gogotsi, Y.; Simon, P. Relation between the Ion Size and Pore Size for an Electric Double Layer Capacitor. *J. Am. Chem. Soc.* **2008**, *130*, 2730–2731.
14. Yang, C.-M.; Kim, Y.-J.; Endo, M.; Kanoh, H.; Yudasaka, M.; Iijima, S.; Kaneko, K. Nanowindow-Regulated Specific Capacitance of Supercapacitor Electrodes of Single-Wall Carbon Nanohorns. *J. Am. Chem. Soc.* **2007**, *129*, 20–21.
15. Simon, P.; Gogotsi, Y. Materials for Electrochemical Capacitors. *Nat. Mater.* **2008**, *7*, 845–854.
16. Lockett, V.; Sedev, R.; Ralston, J.; Horne, M.; Rodopoulos, T. Differential Capacitance of the Electrical Double Layer in Imidazolium-Based Ionic Liquids: Influence of Potential, Cation Size, and Temperature. *J. Phys. Chem. C* **2008**, *112*, 7486–7495.
17. Alam, M. T.; Islam, M.; Okajima, T.; Ohsaka, T. Capacitance Measurements in a Series of Room-Temperature Ionic Liquids at Glassy Carbon and Gold Electrode Interfaces. *J. Phys. Chem. C* **2008**, *112*, 16600–16608.
18. For a recent review on various energy applications of RTILs, see: Wishart, J. F. Energy Applications of Ionic Liquids. *Energy Environ. Sci.* **2009**, *2*, 956–961.
19. Pinilla, C.; Del Pópolo, M. G.; Kohanoff, J.; Lynden-Bell, R. M. Polarization Relaxation in an Ionic Liquid Confined between Electrified Walls. *J. Phys. Chem. B* **2007**, *111*, 4877–4884.
20. Fedorov, M. V.; Kornyshev, A. A. Ionic Liquid Near a Charged Wall: Structure and Capacitance of Electrical Double Layer. *J. Phys. Chem. B* **2008**, *112*, 11868–11872.
21. Huang, J.; Sumpter, B. G.; Meunier, V. Theoretical Model for Nanoporous Carbon Supercapacitors. *Angew. Chem., Int. Ed.* **2008**, *47*, 520–524.
22. Huang, J.; Sumpter, B. G.; Meunier, V. A Universal Model for Nanoporous Carbon Supercapacitors Applicable to Diverse Pore Regimes, Carbon Materials, and Electrolytes. *Chem.—Eur. J.* **2008**, *14*, 6614–6626.
23. Shim, Y.; Kim, H. J. Solvation of Carbon Nanotubes in a Room-Temperature Ionic Liquid. *ACS Nano* **2009**, *3*, 1693–1702.
24. See, for example:Saito, R.; Dresselhaus, G.; Dresselhaus, M. S. *Physical Properties of Carbon Nanotubes*; Imperial College Press; London, 1998.
25. Schmickler, W. Electronic Effects in the Electric Double Layer. *Chem. Rev.* **1996**, *96*, 3177–3200.
26. For the effect of RTIL polarizability on solvent structure and dynamics, see, for example: Yan, T.; Burnham, C. J.; Del Pópolo, M. G.; Voth, G. A. Molecular Dynamics Simulation of Ionic Liquids: The Effect of Electronic Polarizability. *J. Phys. Chem. B* **2004**, *108*, 11877–11881.
27. Canongia Lopes, J. N.; Deschamps, J.; Pádua, A. A. H. Modeling Ionic Liquids Using a Systematic All-Atom Force Field. *J. Phys. Chem. B* **2004**, *108*, 2038–2047.
28. Canongia Lopes, J. N.; Deschamps, J.; Pádua, A. A. H. Modeling Ionic Liquids Using a Systematic All-Atom Force Field. *J. Phys. Chem. B* **2004**, *108*, 11250.
29. de Andrade, J.; Böes, E. S.; Stassen, H. Computational Study of Room Temperature Molten Salts Composed by 1-Alkyl-3-methylimidazolium Cations—Force Field Proposal and Validation. *J. Phys. Chem. B* **2002**, *106*, 13344–13351.
30. Heyes, D. M. Electrostatic Potentials and Fields in Infinite Point Charge Lattices. *J. Chem. Phys.* **1982**, *74*, 1924–1929.
31. Odom, T. W.; Huang, J.-L.; Kim, P.; Lieber, C. M. Atomic Structure and Electronic Properties of Single-Walled Carbon Nanotubes. *Nature* **1998**, *391*, 62–64.
32. Hummer, G.; Rasaiah, J. C.; Noworyta, J. P. Water Conduction through the Hydrophobic Channel of a Carbon Nanotube. *Nature* **2001**, *414*, 188–190.
33. Bonhôte, P.; Dias, A.-P.; Papageorgiu, N.; Kalyanasundaram, K.; Grätzel, M. Hydrophobic, Highly Conductive Ambient-Temperature Molten Salts. *Inorg. Chem.* **1996**, *35*, 1168–1178.
34. Wagner, M.; Stanga, O.; Schröer, W. The Liquid−Liquid Coexistence of Binary Mixtures of the Room Temperature Ionic Liquid 1-Methyl-3-hexylimidazolium Tetrafluoroborate with Alcohols. *Phys. Chem. Chem. Phys.* **2004**, *6*, 4421–4431.
35. Kumar, A. Estimates of Internal Pressure and Molar Refraction of Imidazolium Based Ionic Liquids as a Function of Temperature. *J. Solution Chem.* **2008**, *37*, 203–214.
36. Weingärtner, H.; Knocks, A.; Schrader, W.; Kaatze, U. Dielectric Spectroscopy of the Room Temperature Molten Salt Ethylammonium Nitrate. *J. Phys. Chem. A* **2001**, *105*, 8646–8650.
37. Daguenet, C.; Dyson, P. J.; Krossing, I.; Oleinikova, A.; Slattery, J.; Wakai, C.; Weingärtner, H. Dielectric Response of Imidazolium-Based Room-Temperature Ionic Liquids. *J. Phys. Chem. B* **2006**, *110*, 12682–12688.
38. Halder, M.; Headley, L. S.; Mukherjee, P.; Song, X.; Petrich, J. W. Experimental and Theoretical Investigations of Solvation Dynamics of Ionic Fluids: Appropriateness of Dielectric Theory and the Role of DC Conductivity. *J. Phys. Chem. A* **2006**, *110*, 8623–8626.
39. Stoppa, A.; Hunger, J.; Buchner, R.; Hefter, G.; Thoman, A.; Helm, H. Interactions and Dynamics in Ionic Liquids. *J. Phys. Chem. B* **2008**, *112*, 4854–4858.
40. For the importance of nonlinear electronic polarizability of solvents, see, for example: Bursulaya, B. D.; Kim, H. J. Spectroscopic and Dielectric Properties of Liquid Water: A Molecular Dynamics Simulation Study. *J. Chem. Phys.* **1998**, *109*, 4911–4919.
41. For roles played by solvent quadrupole moments in solvation, see: Jeon, J.; Kim, H. J. A Continuum Theory of Solvation in Quadrupolar Solvents. II. Solvation Free Energetics, Dynamics, and Solvatochromism. *J. Chem. Phys.* **2003**, *119*, 8626–8635, and references cited therein.
42. Stoller, M. D.; Park, S.; Zhu, Y.; An, J.; Ruoff, R. S. Graphene-Based Ultracapacitors. *Nano Lett.* **2008**, *8*, 3498–3502.
43. For RTIL ion conductivity, see: Shim, Y.; Kim, H. J. On Dielectric Relaxation, Ion Conductivity, Solvent Rotation, and Solvation Dynamics in a Room-Temperature Ionic Liquid. *J. Phys. Chem. B* **2008**, *112*, 11028–11038, and references cited therein.
44. Shim, Y.; Kim, H. J. Free Energy and Dynamics of Electron Transfer Reactions in a Room-Temperature Ionic Liquid. *J. Phys. Chem. B* **2007**, *111*, 4510–4519.
45. Lynden-Bell, R. M. Can Marcus Theory Be Applied to Redox Processes in Ionic Liquids? A Comparative Simulation Study of Dimethylimidazolium Liquids and Acetonitrile. *J. Phys. Chem. B* **2007**, *111*, 10800–10806.
46. Annapureddy, H. V. R.; Margulis, C. J. Controlling the Outcome of Electron Transfer Reactions in Ionic Liquids. *J. Phys. Chem. B* **2009**, *113*, 12005–12012.
47. Shim, Y.; Kim, H. J. Adiabatic Electron Transfer in a Room-Temperature Ionic Liquid: Reaction Dynamics and Kinetics. *J. Phys. Chem. B* **2009**, *113*, 12964–12972.
48. Conway, B. E.; Birss, V.; Wojtowicz, J. The Role and Utilization of Pseudocapacitance for Energy Storage by Supercapacitors. *J. Power Sources* **1997**, *66*, 1–14.
49. Nosé, S. A Unified Formulation of the Constant Temperature Molecular Dynamics Methods. *J. Chem. Phys.* **1984**, *81*, 511–519.
50. Hoover, W. G. Canonical Dynamics: Equilibrium Phase-Space Distributions. *Phys. Rev. A* **1985**, *31*, 1695–1697.
51. Forester, T. R.; Smith, W. *DL_POLY User Manual*; CCLRC, Daresbury Laboratory: Daresbury, Warrington, U.K., 2001.